ON THE PERFORMANCE AND FLIGHT MECHANICS ANALYSIS OF DUCTED ROTORS – AXIAL FLIGHT

Maximilian Mindt, DLR (German Aerospace Center), Institute of Flight Systems, Braunschweig, Germany

Abstract

A literature survey on ducted rotors revealed that some operating conditions are not captured yet by modeling efforts using the blade element momentum theory. The principal flow conditions missing a solution are presented and possible application cases are outlined. A unification of the inflow calculation for open and ducted rotors in hover and climb condition is proposed and implemented into the Versatile Aeromechanics Simulation Tool. Wind tunnel data are used to validate the complete model including an airloads calculation based on tabulated airfoil data. Satisfactory performance predictions were obtained in the open as well as the ducted rotor validation except for high thrust levels. Large deviations from test data were observed in the wind speed results using the geometrical contraction factor of the shroud in the simulations, whereas assuming a cylindrical duct yielded a good match. Further investigations are needed to identify whether the formulation basing the flow contraction on geometry is unsuited in general or improves results for other ducted rotor configurations. The application of tip losses onto the inflow instead of as a factor on the airloads leads to a physically more meaningful simulation of the flow field. It also improved the agreement with experimental data for high thrust cases in this study.

NOTATION

Symbols

A	area, m^2
C	coefficient, -
D	propeller diameter, m
d	tip gap, m
E	enforcement factor, -
F	tip loss factor, -
J	advance ratio based on D and RPS, -
K	contraction factor, -
Ma	Mach number, -
Q	torque, N m
R	rotor radius, m
T	thrust, N
v	velocity, $\mathrm{m\,s^{-1}}$
δ	relative thickness, -
η	efficiency, -
μ	advance ratio, -
ρ	density of air, $\mathrm{kg\,m^{-3}}$
Ω	rotational speed of rotor, $\mathrm{rad\,s^{-1}}$

Subscripts

d	design
e	duct exit
h	hover
i	induced
L	lift
max	maximum
P	power
R	rotor plane
T	thrust
∞	freestream component

Acronyms

ADM	actuator disk model
BEMT	blade element momentum theory
CFD	computational fluid dynamics
HSS	high speed shroud
MBS	multi body system
RPS	revolutions per second
TL	tip loss
UAV	unmanned aerial vehicles
VAST	Versatile Aeromechanics Simulation Tool
VRS	vortex ring state

1. INTRODUCTION

In recent years, there has been a sharp increase in the number of concepts as well as flown vehicles in the class of unmanned aerial vehicles (UAV). Use cases range from hobbyist activities to military applications for reconnaissance and attack missions for which they have gained a pronounced role in the current Russia-Ukraine war. The broad range of application scenarios leads to a variety of system architectures. Many concepts feature multiple rotors which are often also ducted.

Additionally, ducted rotors are featured on a multitude of concepts for urban air mobility. In contrast to the UAV, these concepts are supposed to transport one or more passengers in densely populated areas, which entails a much higher burden on load capacity and safety. On top of that, European as well as American military have requirements for an aircraft with vertical take-off and landing but also high-speed flight capabilities. These demands might be solved by compound helicopter concepts as the SB>1 concept of Sikorsky and Boeing, and will possibly feature a ducted pusher propeller. Next to these rather new (re-)applications of the ducted rotor concept, it has been employed as the anti-torque device on many helicopters with conventional main rotor - tail rotor configuration, for example coined the Fenestron on the models of Airbus Helicopters.

Overall, this leads to a broad range of sizes and variants of ducted rotors. A model that is capable of performance prediction for all these incarnations needs to cover a wide range of Reynolds and Mach numbers. While some concepts entail a mainly axial freestream velocity component — as for the pusher propeller — others will operate with varying degrees of tangential flow — as with the anti-torque device. Flight mechanics aspects might lead to additional operating conditions of the rotors that are to be represented. Especially the last point has been neglected in many efforts to model the physics of the ducted rotor with basic principles, as will be shown in this paper.

2. PHYSICS OF DUCTED ROTORS

Many recent investigations of ducted rotors try to capture their physics directly through computational fluid dynamics (CFD) calculations. One area of investigation is the aerodynamic interactions of the complete helicopter with a ducted tail rotor as in the publications of Roh et al. in Ref. 1 and Ref. 2. For the investigations, the tail rotor was modeled via an actuator disk model (ADM) while the main rotor and its wake were resolved in detail. The ADM approach was also used for a ducted pusher propeller in most of the investigations of Zhang in his dissertation (Ref. 3) to study the interference with the main rotor of a helicopter. In the simulations, the pusher was placed at various locations under the main rotor, which was either modeled via a non-uniform ADM, or non-uniform actuator lines for the blades.

Other recent investigations were focused on the aeroacoustics of a ducted fan. In order to capture the detailed mechanisms of noise generation, the ducted rotor was resolved in detail with its rotating blades. This method was employed by Sun et al. in Ref. 4 to compare the CFD results to particle image velocimetry results of a ducted rotor test stand. Stadlmaier et al. also used this approach to simulate the tail section of a helicopter including the ducted fan in Ref. 5.

While these investigations provide the opportunity to get a detailed view and understanding of the mechanisms involved, they are also computationally very expensive. Therefore, they are not applicable in the preliminary design process or for broad flight mechanics investigations, were a large number of variants and conditions needs to be computed in a short time frame. For these tasks, models based on the blade element momentum theory (BEMT) are commonly employed for ducted rotors.

The base of this theory is that by the conservation of momentum, the thrust generation of a rotor is enabled by pushing down the surrounding air, assuming the rotor plane to be an actuator disk without detailed resolution of the blades. The principle was used by Glauert already in 1926 (Ref. 6) to explain the functioning of the autogyro. The theory has first been extended by Gustafson and Gessow in Ref. 7 to incorporate the actual geometry and aerodynamic characteristics of the blades, which is eponymous for the “blade element” part of the BEMT.

For open rotors, three operating states of the rotor are identified: the hover and climb case, represented in the left sketch of Figure 1, the fast descent, shown on the right, and the vortex ring state (VRS), shown in the middle of Figure 1. The latter is characterized by reingestion of the rotor’s wake into the rotor plane, which leads to unsteady behavior and prevents an analytic description via momentum theory. Therefore, rather than a physical description, this range is often described via the approximate mean experimental results of the induced velocities as for example provided via a polynomial by Leishman in section 2.13 of Ref. 8.

Since the derivations of the two analytically captured operating states are available in a multitude of textbooks like the one of Leishman (Ref. 8), the reader is referred to these for details. Resulting equations that are useful for the understanding of similarities and differences to ducted rotors are shortly introduced in the following, though. In axial climb, a freestream velocity v_∞ is encountered by the rotor from above, as shown in the left sketch of Figure 1. The induced velocity in the rotor plane v_i is computed as:

$$v_i = -\frac{v_\infty}{2} + \sqrt{\frac{{v_\infty}^2}{4} + \frac{T}{2\rho A_R}} \tag{1}$$

with the thrust T, density ρ and rotor area A_R. Without v_∞, i.e., in hover, the equation simplifies to

$$v_{i,h} = \sqrt{\frac{T}{2\rho A_R}}. \tag{2}$$

The total velocity observed in the rotor plane v_R is the sum of the induced velocity and the freestream velocity:

$$v_R = v_i + v_\infty \tag{3}$$

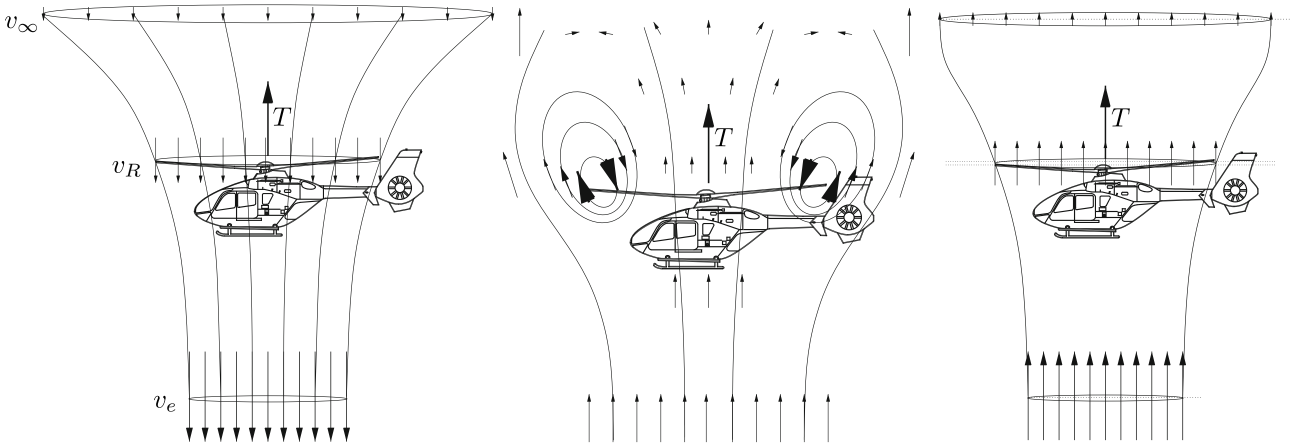

Figure 1: Momentum theory operating conditions for an open rotor: hover and climb (left), vortex ring state (mid) and fast descent (right), adapted from Ref. 9

and respectively for v_e of the plane far below the rotor

$$(4) \qquad v_e = v_{i,e} + v_\infty.$$

The relation of v_i to $v_{i,e}$ reads:

$$(5) \qquad v_{i,e} = 2v_i.$$

For a rotor enclosed by a duct as sketched in Figure 2, the flow will follow the contour of the duct if the change in cross section is not too sharp or other factors like an adverse pressure gradient preclude this. Due to conservation of mass, the mass flow will remain constant: $\rho A v =$ const. A direct relationship between the velocity in the rotor plane v_R and in the duct exit plane v_e follows:

$$(6) \qquad \rho A_R v_R = \rho A_e v_e \rightarrow v_e = \frac{A_R}{A_e} v_R = K v_R$$

The second equality introduces the contraction factor K. It can be inferred that the ratio v_e/v_R will be smaller than the factor of two observed for the open rotor in hover in combination of Eq. (4) and Eq. (5). Ducted anti-torque devices are often equipped with a widening duct or diffusor, as sketched in Figure 2, so that the contraction factor will even be smaller than one.

The extension of the BEMT methodology for use with ducted rotors can be found in several publications, to different extent. In Leishman's textbook (Ref. 8) in section 6.10, only the hover case is covered and a wake contraction parameter $a_w = 1/K$ is used in the derivations. Kothmann captures the climb as well as the hover condition in the ducted rotor model of his dissertation (Ref. 10), but only considers a duct of constant cross section. Varying cross sections in combination with freestream flow encountered by the rotor are treated by Pereira in his dissertation (Ref. 11), by Stahlhut in Ref. 12, and in the dissertation of Krämer (Ref. 13). The latter focuses on the identification of values for parameters incorporated into the physically motivated sub-models of the complete ducted rotor - stator - shroud model with the hope

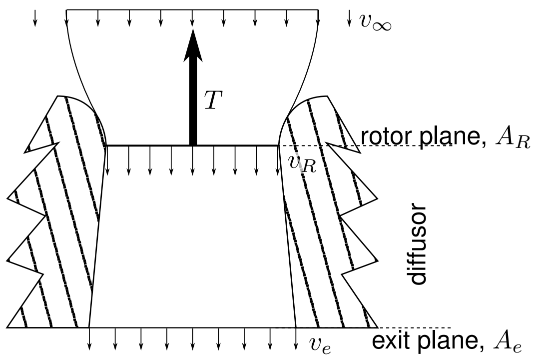

Figure 2: Momentum theory representation of a ducted rotor in hover and climb operating condition

on physical insight, and leaves K open for optimization. However, parameter sets based on two flight test campaigns of the same helicopter yield diametral force contributions of the sub-components.

The model proposed by Bölk et al. in Ref. 14 builds on an extended momentum theory solution that is valid for non-axial flow conditions. Instead of a physically motivated derivation of the extension to ducted rotors, correction factors are applied on the freestream components and the induced velocity in the rotor plane. Additionally, a thrust share factor that describes the relation between rotor thrust and total thrust is derived from measurements. By making the inflow correction factor and the thrust share factor dependent on wind speed and thrust, the inference on flow physics is reduced.

As for the open rotor, the velocities observed in the rotor plane and far below the rotor are the sum of the induced velocity in the respective plane and the freestream velocity, see Eq. (3) and Eq. (4). Therefore, the freestream flow that needs to pass the duct will also slow down through the expanding cross section in the case of a diffusor as shown in the sketch in Figure 2. This effect is also represented in the ducted BEMT models of Pereira (Ref. 11) and Stahlhut (Ref. 12). On the other hand, Krämer (Ref. 13) uses K for the induced velocity only. This would be explicable by his use of K as an optimization parameter that is not fixed to geometry. However, K would then need to be dependent on axial velocity of the rotor, whereas it is only dependent on forward flight velocity of the helicopter, translating to mostly tangential flow on the ducted tail rotor in the model. Since Kothmann (Ref. 10) only considers the cylindrical ducted rotor, K is not part of his formulation.

If the flow follows the contour of the duct as in the sketch in Figure 2, the induced velocity can be derived as

$$v_i = -v_\infty + \frac{1}{K}\sqrt{{v_\infty}^2 + \frac{2T}{\rho A_R}}. \tag{7}$$

In hover and with a cylindrical duct, this reduces to

$$v_{i,h} = \sqrt{\frac{2T}{\rho A_R}}. \tag{8}$$

Comparing this to Eq. (2) shows that the induced velocity of the cylindrical-duct rotor is twice that of the open rotor with the same thrust generated.

For the open rotor, the stream tube contracts less with increasing axial freestream flow, whereas the duct enforces a constant area ratio or contraction factor regardless of v_∞. The fixed area ratio of the flow may lead to unexpected results, especially for high flow velocities and relatively low thrust conditions. In the border case without thrust and $K = 2$, i.e., a funnel, v_i will become $-v_\infty/2$, which is notably negative. This is because the flow decelerates in front of the narrowing duct and the induced velocity is by definition the difference with respect to the ambient velocity. At the duct exit, the flow has accelerated back to v_∞, governed by the result of the conservation of mass of Eq. (6).

The terms of Eq. (1) and Eq. (7) for the induced velocities are very similar, especially if $K = 2$ is defined for the open rotor, based on Eq. (5). Then, the only remaining difference is in the first term of the equations. By introduction of an enforcement factor E with

$$E = \begin{cases} 2 & \text{open rotor} \\ 1 & \text{ducted rotor with enforced area ratio} \\ K & \text{ducted rotor, no enforced area ratio} \end{cases} \tag{9}$$

a unified formula for v_i, usable for open and ducted rotors, can be established:

$$v_i = -\frac{v_\infty}{E} + \frac{1}{K}\sqrt{{v_\infty}^2 + \frac{2T}{\rho A_R}}. \tag{10}$$

The third option for E is introduced to allow replication of the formulation of Krämer. It translates to the enforcement of the area ratio of the duct only for v_i and not for the freestream component.

Concerning the reversed flow condition, Ref. 10 as well as Ref. 13 assume that the behavior is symmetrical by taking the absolute value of the sum of freestream velocity and induced velocity as relevant. Comparing the sketch of Figure 3 to that of Figure 2 clearly shows the differences in flow structure, though. While the flow is constrained by the geometry of the duct after passing the rotor plane in the hover and climb case, the oncoming flow is constrained in the fast descent state. Due to the sharp edge that the flow encounters while entering the duct, it can not be assumed that the flow still has freestream velocity. This leads to a fourth relevant velocity compared to the three velocity planes necessary to describe the flow in the climb case, making the analytical solution of this state more complex. The solution approaches found in the literature do not represent the difference in flow structures between descent and climb case, though.

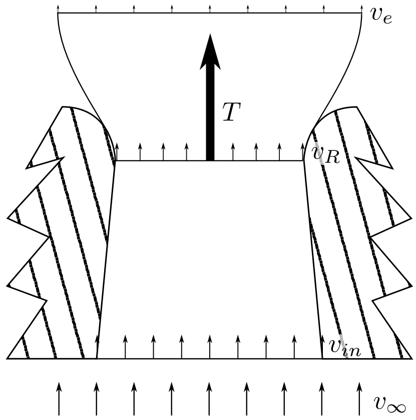

Figure 3: Momentum theory representation of a ducted rotor in fast descent operating condition

In the models mentioned above, the VRS has not been addressed except by Krämer, who states that due to the duct allowing only flow in either direction, a defined flow state is always present. His reversed flow formulation directly starts where the hover and climb state ends. Contrary to this, a recent study found that the VRS is indeed obtainable for ducted rotors as well, the vortex ring just formed around the outside of the duct in the experiments conducted by Pickles et al. (Ref. 15). The extent to which the formation of a vortex ring is possible strongly depends on the dimensions of the duct as well as the presence of other components in the vicinity of the rotor like the fin for a ducted tail rotor, so a generic treatment of this case is likely to be even more difficult than it is for the open rotor.

In Figure 1, the thrust is always assumed to point "upwards", and the induced velocity opposite to that. If the thrust changes direction – which is not a common case for the main rotor, but may occur on a tail rotor or a generic steering device – the wake tube is inverted and the corresponding definitions need to be adapted as well. Starting with an open rotor in a climb case, after a change of the thrust direction either the fast descent state or vortex ring state is attained, depending on the magnitudes of the freestream flow and the generated thrust. For the ducted rotor, the situation is a bit more complex, as shown in Figure 4 and Figure 5. If the thrust direction is reversed, the thrust is generated in the direction of the diffuser. In the case shown in Figure 4 which

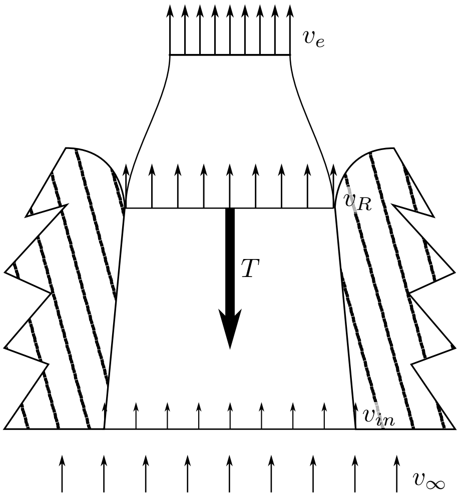

Figure 4: Momentum theory representation of a ducted rotor in thrust reversal

is denoted by “thrust reversal”, the oncoming flow cannot develop freely, but is constrained by the diffusor’s geometry. On the other hand, the flow can develop freely after passing the rotor plane. As with the fast descent case, four planes with relevant velocities are identified. A possible use case for the thrust reversal exists with a ducted tail rotor when a fast pirouette is commanded in hover. Another use case is in fast forward flight, where the tail rotor is unloaded, thus necessitating a reversed thrust if a yaw maneuver is commanded.

The apparent difference in the flow structure due to a change of the thrust direction was not addressed explicitly in the models found in literature. This can in part be attributed to the models’ area of application: Pereira employed the model for lift generating micro air vehicles (Ref. 11) and Stahlhut’s intended application were pusher propellers (Ref. 12).

The second possible flow condition with thrust generated in diffusor direction is shown in Figure 5 and shall be referred to as “fast descent type 2”. In this case, the constraint on flow development is apparent after the flow passes the rotor plane. Apart from the direction of the thrust, the boundary conditions are very similar to the hover and climb case of Figure 2, especially that there are only three velocity planes necessary to describe the flow. The implementation of this working state has also not been found in the literature, despite possible corner use cases for pusher propellers. The fast descent type 2 condition can occur with a too low pitch or rotational speed setting in fast forward flight or when using the propeller for deceleration. A ducted wind turbine is also operating in this working state.

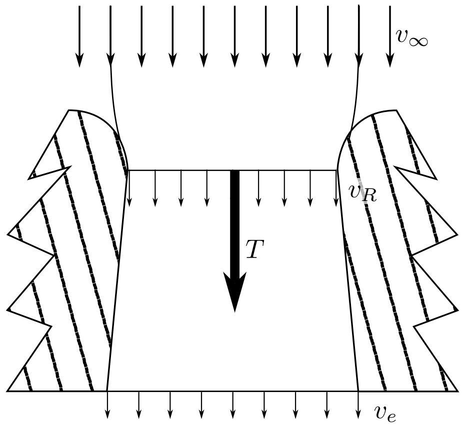

Figure 5: Momentum theory representation of a ducted rotor in fast descent type 2

3. IMPLEMENTATION

The BEMT approach has been implemented in a very generic way in the Versatile Aeromechanics Simulation Tool (VAST). This tool is currently under development at DLR’s Institute of Flight Systems and Institute of Software Technology, and is described in detail in Ref. 16. The implementation assumes that the BEMT equations for thrust and torque, or axial and tangential induced velocity, respectively, can be applied in annular rings independently from each other. VRS conditions can be treated via the polynomial provided by Leishman (Ref. 8, section 2.13) or via an alternative formulation proposed by Buhl in Ref. 17. Buhl’s solution aims at more accurately representing the transition from the fast descent into the VRS regime. It is not suited for calculation of induced velocities in the whole range from hover to fast descent, though.

If the direction of thrust changes, the underlying coordinate definitions are switched automatically to conform with the flow state definitions according to BEMT as outlined in the last section. Together with the implementation of the unified formulation for open and ducted rotors introduced above in Eq. (10), all possible operating states of open rotors are captured. A verification of the fast descent state implementation for the open rotor has been conducted recently via a comparison with results of CFD calculations and with a VAST internal vortex theory inflow model in Ref. 18. For the ducted rotor, hover and climb as well as the fast descent type 2 condition are available.

The loss of lift at the blade tip due to the tip vortices, coined as tip loss (TL), can be calculated via the models of Prandtl, originating in Ref. 19, or Goodman, as derived in Ref. 20. Prandtl’s formulation is widely used in applications of the BEMT. VAST provides the options to use it in its original form, depending on the blade tip inflow angle, or using the local inflow angles of the individual blade elements which is a variation often used but not substantiated by theory. Goodman also derived his TL formulation based on vortex sheets stacked downstream of the rotor plane, but accounting for the fact that the presence of a wall next to the rotor obstructs the vortex-induced flow around the blade tip. For a large distance of blade tip and duct wall, coined tip gap d, of a ducted rotor the result approaches that of the Prandtl TL. For $d \to 0$, the loss factor F approaches one, representing no loss. F was initially implemented in VAST as a factor lowering the lift force of the blade element. During usage of the model it became apparent that this leads to unphysical effects, so the consideration of TL in the induced velocities was investigated as well. Equation 10 then is extended to:

$$v_i = -\frac{v_\infty}{E} + \frac{1}{K}\sqrt{{v_\infty}^2 + \frac{2T}{\rho A_R F}}. \tag{11}$$

For the ducted rotor investigations presented below, the option $E = 1$ as substantiated in section 2 is used, and $E = 2, K = 2$ is used for the open rotor calculations.

The choice of where to employ the tip loss exists in VAST because the blade element and the momentum theory parts of the BEMT formalism are not equated and solved for prior to implementation as it is done in many realizations of the BEMT method, for example in Ref. 12. In VAST, the airloads calculation, the blade element kinematics, and the inflow calculation take place in different models, and their mutual interaction is solved numerically and iteratively during each simulation step. This way, the different components of the calculation can be exchanged easily, allowing for switching of fidelity levels. The aerodynamics of rotor blades for example can be captured in a range from steady (quasi-) linear airloads to a semi-empirical analytical model incorporating dynamic stall and the effects of yawed flow, as detailed in Ref. 21. For the investigations presented below, a table lookup model was employed for the different airfoils. The calculation of structural dynamics and kinematics are facilitated by a multi body system (MBS) model, which is only used to provide rigid and prescribed kinematics in the setup described below. The MBS capabilities of VAST would also permit to simulate structural flexibility of the blades with special focus on dynamic effects caused by the rotor rotation. Details on this can be found in Ref. 22.

4. VALIDATION

4.1. Wind Tunnel Data

A validation campaign for the implemented BEMT model was performed using the data published by Grose in Ref. 23. In the tests, a ducted rotor was measured in a wind tunnel for static performance as well as with axial wind speeds up to a Mach number of $Ma = 0.6$, representing a ducted pusher propeller. The data set also covers a wide range of rotor speeds and pitch settings. For the test points with wind speed, the minimum rotational speed Ω per pitch setting was that for zero thrust, and the maximum speed Ω_{max} was determined either by the constraints of the motor or reaching the maximum measurable thrust level. Different advance ratios $\mu = V_\infty/\Omega R$ were established for every wind speed by variation of Ω. Supersonic flow conditions were apparent next to the blade tip at Ω_{max}.

The tested propeller has four blades with a radius R of 0.381 m and features a $25\,\%\,R$ root cutout. The blades have a constant chord length of $c = 0.116$ m and a nonlinear twist ranging from $41\,°$ at the root to $13\,°$ at the blade tip. The pitch angle at $75\,\%\,R$ is used for the blade pitch setting denomination in the report and in the figures below. The visual representation of the open rotor model in the VAST graphical user interface is shown in Figure 6. Note that a generic airfoil shape is used to represent the geometry of aerodynamic sections in the VAST visualization, i.e., the actual relative thickness δ is not shown, but the twist and dimensions are reflected. Only δ and the design lift coefficient $C_{L,d}$ distributions over radius are given in the report instead of the airfoils employed. Therefore, publicly available airfoil polar data that closely fit to these parameters were chosen. The airfoil distribution employed, from blade attachment to the tip, is given in Table 1. For blade element collocation points lying between the ranges of a single airfoil, the results of the airloads calculations of the adjacent airfoils are interpolated linearly. A convergence study showed that when the blade elements are distributed such that the same annular ring area is swept by each element during a revolution, ten radial blade segments are sufficient.

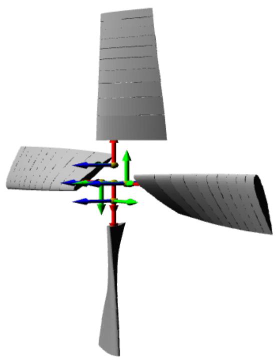

Figure 6: Representation of the open rotor wind tunnel model in the VAST graphical user interface

Two different shroud configurations were investigated, one with a rounder inlet for better hover performance and the other one having a sharper leading edge, designated high speed shroud (HSS). The length of the

Airfoil	$\delta, \%$	radial station, $\%R$
NACA2421	21.0	0.250 - 0.281
OA213	12.5	0.334
OA209	9.0	0.412
GOE55	6.2	0.526
GOE427	4.6	0.650
NACA SC(2)-0403	3.0	0.880 - 1.000

Table 1: Distribution of airfoils over radius

shroud chord is equal to the propeller radius, and the rotor plane is situated at mid-chord of the shroud. The tip gap is $d = 0.006\,35\,\mathrm{m} = 1.67\,\%\,R$. Based on the shroud exit area $A_e = 0.508\,\mathrm{m}^2$, the contraction factor is $K = 0.897$.

In Ref. 23 the data are presented in the form of thrust coefficient C_T and power coefficient C_P for the static cases, and as C_P and efficiency η for the cases with wind speed. Since in the report, $\eta = {}^{C_T J}/_{C_P}$ with J being the advance ratio based on revolutions per second (RPS) and propeller diameter D, errors in power prediction as well as thrust prediction are propagated when comparing simulation results to this measure. Therefore, C_T values were extracted from the η data. As another side note, the dimensionless performance coefficients were computed based on D and RPS in the report, but the definitions commonly used for helicopters are being used for the display of the results in this paper, i.e.,

$$C_T = \frac{T}{\rho A_R (\Omega R)^2} \tag{12}$$

and using the rotor torque Q:

$$C_P = \frac{Q\Omega}{\rho A_R (\Omega R)^3}. \tag{13}$$

4.2. Static Results

All wind tunnel tests in Ref. 23 were additionally performed without the duct, allowing for evaluation of the effects of the duct. A second benefit is that the implementation of the widely used formulation for open rotors can be checked and used as a baseline for the discussion of the extension to ducted flow.

Open Rotor

Figure 7 shows the thrust coefficient of the open propeller for varying blade pitch angles and rotational speeds. As in all following figures, points and curves of the same color pertain to the same pitch angle, indicated in the legend next to the diagram, dots mark experimental measurements, and the line style pertains to different calculation options in VAST.

The test data show an increase in C_T with Ω that is not captured by the VAST calculations. This can partially be attributed to the fact that apart from the ONERA 2-series airfoils, no Mach number dependency is accounted for in the polar tables used. In reality, airfoil parameters such as the lift curve slope $C_{L,\alpha}$ are found to be increasing with Mach number. This can be modeled by the so called Prandtl-Glauert correction published by Glauert in Ref. 24:

$$C_{L,\alpha} = \frac{C_{L,\alpha,Ma=0}}{\sqrt{1 - Ma^2)}}. \tag{14}$$

Since this correction only applies to $C_{L,\alpha}$ in linear airfoil behavior, it is not easily applied to tabulated airfoil data. For tabulated data as used in this simulation campaign, the respective airfoil behavior at different Mach numbers would need to be gathered via CFD simulations or wind tunnel measurements. Note that a quadratic increase of thrust with Ω is predicted by the VAST calculations nevertheless, as C_T in Eq. (12) is based on the square of tip speed.

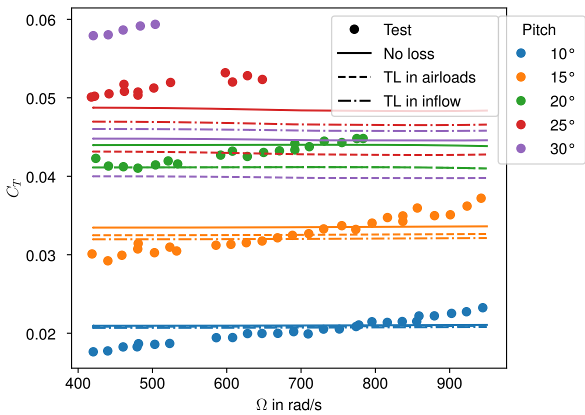

Figure 7: Thrust coefficient of open propeller in static condition

For pitch angles $\theta = 10°$, $15°$, and $20°$, the average thrust is predicted very well by VAST, but too low C_T levels are produced for higher θ. As some airfoil sections are stalling in the calculations but the test results show an unperturbed increase in thrust, the airfoils used in the test may have higher maximum lift capabilities than the polars used in the simulation. Looking closer at the red $25°$ pitch curves, a particularly high tip loss is predicted when the tip loss is applied onto the airloads (dashed line) compared to a calculation with no loss (solid line). In this case, the application of F directly onto the airloads leads to a low thrust value transferred to the inflow calculation which in turn leads to a small inflow velocity. Hence, the angle of attack α at the blade tip is hardly reduced from the high values produced by the large pitch setting. This in turn leads to a higher F calculated for all radial sections of the blade. The prediction of low inflow at the blade tip is not consistent with the effect of flow around the tip that the formulation tries to capture. Applying F in the inflow leads to a much smaller decrease in thrust in this case, as seen in the dash-dot line. A higher inflow is generated when the tip loss is applied in the inflow calculation, fitting to the assumptions. In this case, it is leading to overall smaller Fs because of the smaller tip inflow angle.

For the highest pitch setting of $\theta = 30°$, even a higher thrust is computed with *TL in inflow* than without TL. Here, the high inflow values tend to reduce the angle of attack so far that the airfoils do not operate in fully stalled condition – as without loss and with *TL in airloads* – but in higher lift regimes.

All observations made for the thrust comparison also apply to the validation of static power prediction, as shown in Figure 8: the power level is captured well for $\theta = 10°$, $15°$, and $20°$, but the increase with Ω is missing. The increase in C_P with θ is under-predicted for 25° and heavily underpredicted for 30°, and usage of *TL in inflow* increases the power with respect to calculation without loss for the highest setting.

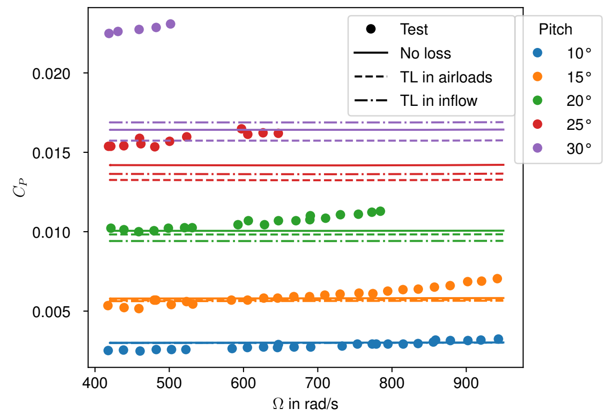

Figure 8: Power coefficient of open propeller in static condition

Ducted Rotor

For the evaluation of the static performance of the ducted propeller, two configurations are available from the experiment: the “static” and the HSS shroud. Evaluation of oil flow patterns on the HSS shroud indicated flow separation directly at the sharp leading edge of the shroud, though. This explains the measured small contribution of thrust by the shroud which is shown in Figure 28 of Ref. 23, and makes the test data unsuitable for evaluation with ducted BEMT, which assumes attached flow. Hence, the “static shroud” data are used for validation of the static performance, assuming a cylindrical duct, i.e., $K = 1$.

The measured C_T is shown in Figure 9 alongside the VAST results for the open rotor in solid lines, ducted rotor with *TL in airloads* in dashed lines, and ducted rotor with *TL in inflow* in dash-dot lines. Goodman’s formulation incorporating the actual tip gap width is used for the ducted rotor simulations, while the results for the open rotor are generated using the Prandtl tip loss. The open rotor results are only shown to quantify the influence of the duct on rotor performance. It can be seen that the results of the ducted simulations are too low throughout, but that the deviation from test data is much smaller with ducted formulation than using the open rotor modeling. Using the latter, the thrust is predicted much higher than

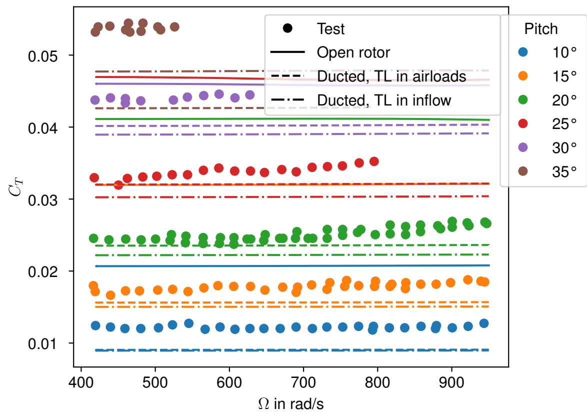

Figure 9: Thrust coefficient of ducted propeller in static condition

experienced. Taking the $\theta = 15°$ data as example the underprediction of the ducted model is $12\,\%$ while the overprediction is $88\,\%$ for the open rotor. The underprediction of VAST is largest at the lowest pitch setting. At the lower two pitch angles, the relative thrust contribution of the shroud was lower than expected with momentum theory, as shown in Figure 28 of Ref. 23, deviating from the other pitch settings in this regard. A higher error of the simulation – which assumes momentum theory behavior – can therefore be expected for $\theta = 10°$. This deviation did not show up in the validation of Stahlhut in Figure 6 of Ref. 12, however. At $\theta = 35°$, the effect of heavily decreased tip loss using the *TL in inflow* method can be seen for the Goodman formulation of the ducted rotor, consistent with the open rotor findings for Prandtl and *TL in inflow*.

The better fit with wind tunnel data using the ducted rotor model is also visible in the static power diagram of Figure 10. The underprediction of VAST is smaller than for C_T, and a big increase towards the test results in power using *TL in inflow* can be seen for the highest pitch.

Overall, the main effect of the presence of a duct on rotor performance is the increase of induced velocity in the rotor plane. This in turn leads to lower thrust (and power) of the rotor at the same pitch setting, and postpones the stall to higher θ. Both effects were reproduced in the VAST simulations, with the shift of the stall augmented

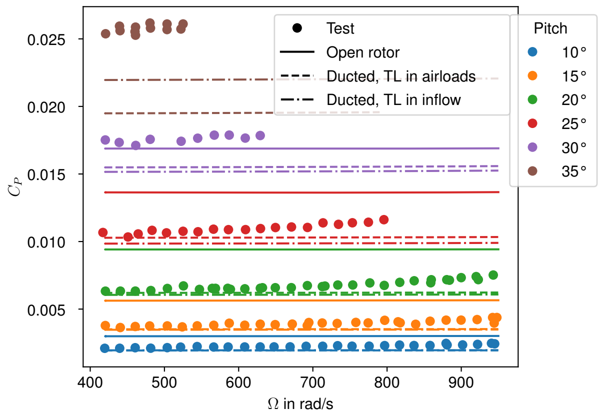

Figure 10: Power coefficient of ducted propeller in static condition

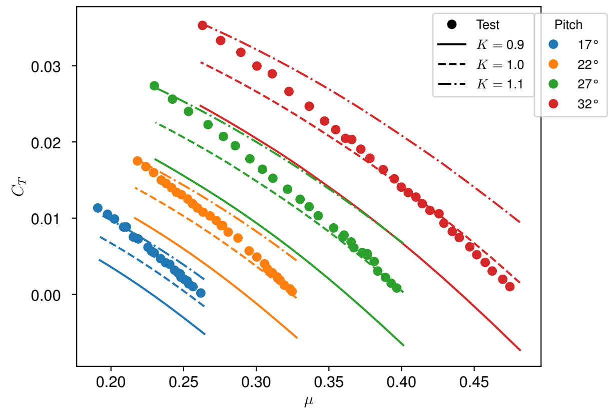

Figure 11: Thrust coefficient of ducted propeller at $Ma = 0.2$ axial wind speed

by application of *TL in inflow*. Due to the better fit of the simulated flow field to the assumptions, as well as influencing the results towards the test data, this tip loss variant will be treated as the default option in the following cases with axial wind speed.

4.3. Wind Speed Results

Tests of the ducted propeller with wind speeds of $Ma =$ 0.2, 0.3, 0.4, 0.5, and 0.6 perpendicular to the rotor plane were performed in the wind tunnel campaign. Figure 11 shows the test results of C_T for $Ma = 0.2$ next to VAST results for different prescribed contraction factors K. As stated in section 4.1, the geometry of the duct translates to a K of 0.9. A substantial offset of the simulation from test data for all advance ratios and increasing with θ can be seen for this value of K, however. With $K = 1$ – the value suited for the cylindrical duct – used in the simulation, the fit to experimental data is much better. The results of $K = 1.1$ are shown as well to better highlight the trend with contraction factor.

In section 2 the physical significance of the hover and climb BEMT extension in the case of $T = 0$ was detailed. An appropriate modeling should be able to yield $T = 0$ correctly, where almost no velocity is induced by the rotor and the difference between v_R and v_∞ is caused by the duct alone. It seems like the idealized assumption of the flow accelerating on its own accord to be expanded to v_∞ again in the duct is unjustified, and may be explained by the associated adverse pressure gradient in the case of zero thrust. Additionally, the results suggest – at least for this test setup – that this not only holds next to $T = 0$, but for all thrusts, advance ratios, pitch settings, and Mach numbers. A possible explanation for this deviation from theory is an at least partial separation of the flow from the duct downstream of the rotor. Interestingly, Stahlhut (Ref. 12) developed the ducted BEMT formulation with incorporation of the effect of K in axial flow in a similar manner as this paper, but no vertical offset exists in his validation of the cases with wind tunnel speed. A too shallow slope of the single C_T curves as well as the slight overprediction of C_T for the highest pitch angle are apparent in his results for $Ma = 0.2$ in Figure 12 of Ref. 12 as well, however.

For the subsequent investigations, $K = 1$ is assumed to fit for modeling the effect of the duct for this configuration. A good match to test data is observed in the high μ range of every pitch setting, with a slight overprediction for the highest pitch of $\theta = 32°$. With decreasing μ, corresponding to higher Ω, the underprediction increases. This may partially be attributed to the missing increase of C_T with Ω already observed in the static tests with the open as well as the ducted rotor.

The observations made regarding the thrust coefficient also hold for C_P, as presented in Figure 12: the $K = 1$ results match well with test data in the high μ range of every θ setting, but underpredict the power for low μ.

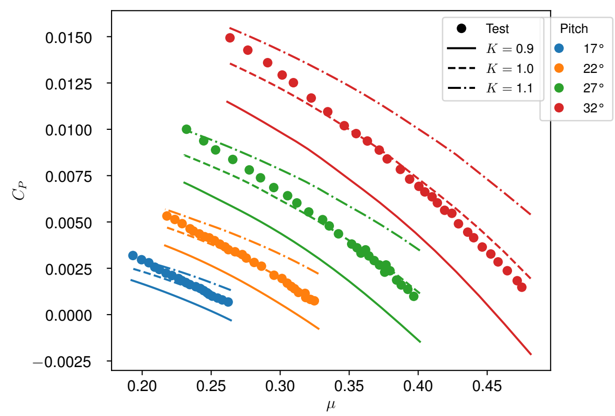

Figure 12: Power coefficient of ducted propeller at $Ma = 0.2$ axial wind speed

The general findings of the $Ma = 0.2$ case can be transferred to the C_T results at $Ma = 0.3$ axial wind speed in Figure 13, and to the C_P results in Figure 14. The wind tunnel results are compared to VAST calculations with different tip loss options. Application of F in the inflow instead of the airloads leads to slightly smaller C_T for the lower two θ at low μ, approximately no difference for $\theta = 37\,°$, and a considerable increase of C_T for the highest pitch. The latter substantially reduces the deviation from test data. Additional computations using *Prandtl in inflow* are shown to substantiate the need to extend the TL description to the computationally more expensive Goodman model. The comparison of the *Goodman in inflow* curves with the *Prandtl in inflow* curves shows that already at the low θ, high C_T points, a considerably higher loss is computed with Prandtl. The reduction of tip losses with Goodman's formulation and the application of F in the inflow model has a significant influence and stresses the usefulness of this adaptation.

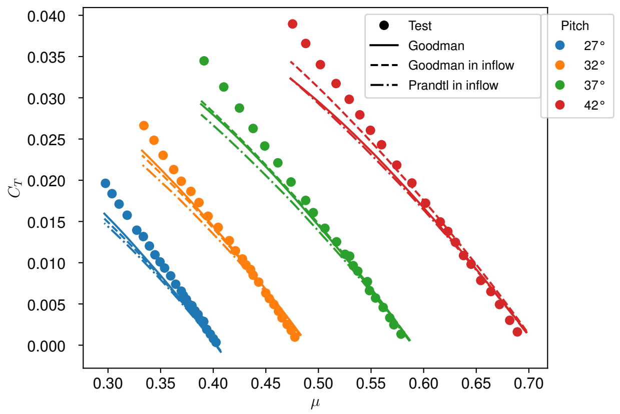

Figure 13: Thrust coefficient of ducted propeller at $Ma = 0.3$ axial wind speed

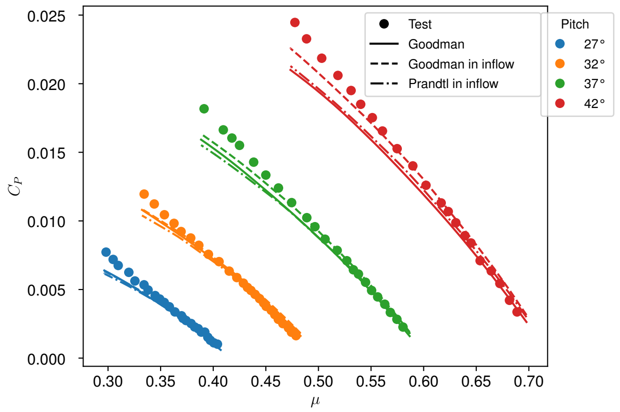

Figure 14: Power coefficient of ducted propeller at $Ma = 0.3$ axial wind speed

C_P is less affected by the variation of the inflow model options, as presented in Figure 14. For the highest pitch, the power is matched much better with application of the Goodman tip loss in inflow, though.

Figure 15 shows the validation of the C_T prediction for the ducted rotor at $Ma = 0.4$. For this wind speed, the ducted formulation is compared to the open rotor simulation results again to evaluate the influence of the duct for high axial wind speeds. The underprediction in high thrust regions known from the other wind speeds is also apparent for the ducted rotor for all except the highest pitch setting. There, an overprediction at low thrust levels together with the too shallow slope of the curve lead to a good fit with experimental results at high C_T, which is rather by concurrence of countering effects, not due to better replication of the physics.

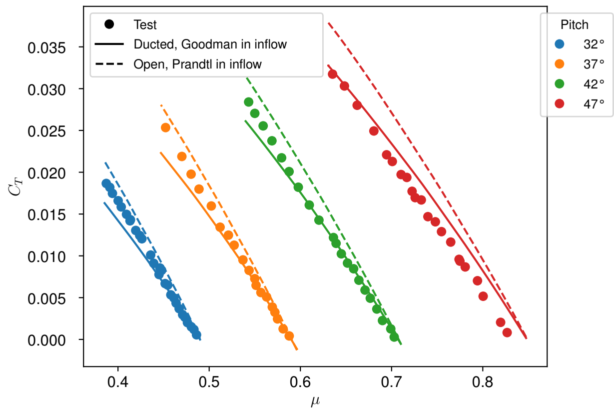

Figure 15: Thrust coefficient of ducted propeller at $Ma = 0.4$ axial wind speed

The usage of the open rotor formulation yields too high thrust values, but the extent of the deviation is much lower than observed for the static case. Taking the highest C_T values at $\theta = 42\,°$ as example, the difference between experimental results and the ducted model is $-7.8\,\%$, and for the open model it is $10.9\,\%$. This shows that the influence of the duct on rotor performance reduces with wind speed, as the induced velocities that are affected by the duct are decreasing. Nevertheless, it is expected that the overprediction of the open rotor model will grow when the airfoil polars are extended to capture Mach number effects, leading to an increase of computed C_T for high Ω.

The power predictions of the ducted rotor at $Ma = 0.4$ axial wind speed are shown in Figure 16. The agreement with all wind tunnel data is better than for the other wind tunnel speeds, except for the lowest pitch with lowest μ. Too high power coefficients are calculated by the open rotor model, fitting to the overprediction of C_T.

Contrary to the lower wind speeds, the slopes of the C_T curves in Figure 17 and of the power curves of Fig-

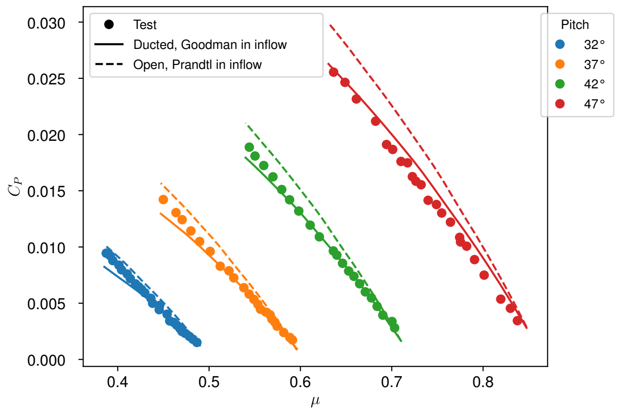

Figure 16: Power coefficient of ducted propeller at $Ma = 0.4$ axial wind speed

ure 18 match well with test data for the highest speed setting of $Ma = 0.6$. At the two higher pitch settings, a vertical offset of predicted thrust is observed, which is more pronounced for the highest pitch. This is an increasing trend, as a small offset is visible in the highest θ curve in the $Ma = 0.4$ results already (Figure 15), and an intermediate offset is apparent in the simulations for $Ma = 0.5$, which are not included in the paper. Corresponding to the overpredicted thrust values, the power coefficients are also overpredicted for the high pitch angles.

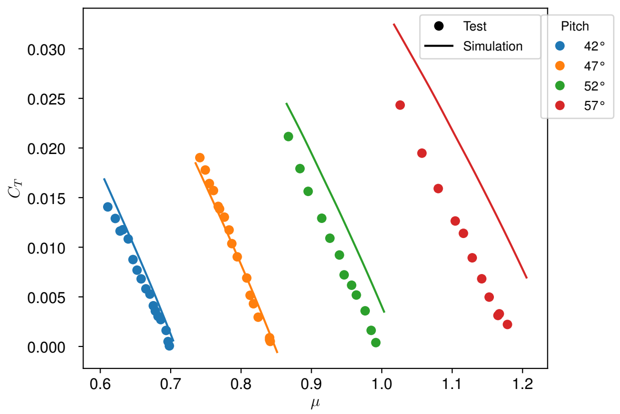

Figure 17: Thrust coefficient of ducted propeller at $Ma = 0.6$ axial wind speed; simulation with *Goodman in inflow* and $K = 1$

5. CONCLUSIONS

A comparison of the physics of open and ducted rotors showed that while the open rotor's three operating conditions are captured well in the literature, models that

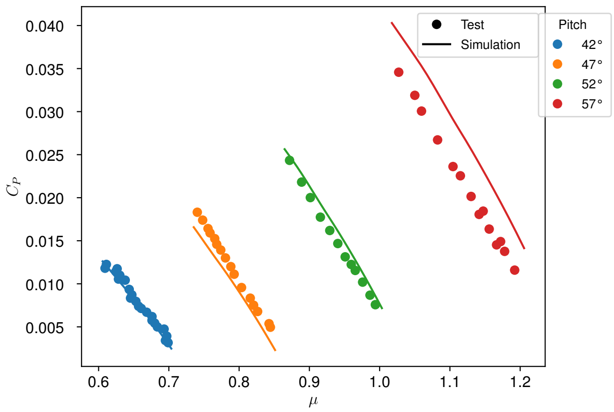

Figure 18: Power coefficient of ducted propeller at $Ma = 0.6$ axial wind speed; simulation with *Goodman in inflow* and $K = 1$

use the BEMT formulation for ducted rotors seem to only address one of the operating states. Due to additional constraints emerging for some of those operating states, an analytical solution for those is more complex and still missing. A general treatment of the VRS regime may be difficult due to the dependence on additional factors like the geometrical arrangement of the duct and other components, and a lack of test data.

The paper presents a unified formulation for the inflow of open and ducted rotors in hover and climb condition. The complete rotor model including rigid body kinematics and airloads calculation based on tabulated airfoil data was validated for axial flow based on a wind tunnel campaign. The following main findings were gathered in this paper:

1. The main influence of the presence of a duct on rotor performance is the increase of induced velocity in the rotor plane. This in turn leads to lower thrust of the rotor at the same pitch setting, and postpones the stall to higher pitch angles. The additional benefit of thrust generation by the shroud is not investigated by this paper.

2. Inclusion of the effects of Mach number variation on airfoil polar data into the simulation should be investigated.

3. Apart from the missing Mach number dependency, satisfactory performance results were obtained in the open as well as the ducted rotor validation.

4. Using the contraction factor given by the geometry of the shroud in the simulations lead to large deviations from test data, whereas using the cylindrical duct value yielded a good match. Further investigations are needed to identify whether the formulation is unsuited in general or improves results for other

ducted rotor configurations, ideally with other geometrical contraction factors, including greater than one.

5. The application of tip losses onto the induced velocities instead of the airloads leads to a physically more meaningful simulated flow field. It also improves the match with experimental data for high thrust cases.

Author contact:
Maximilian Mindt Maximilian.Mindt@dlr.de

6. ACKNOWLEDGEMENTS

The work presented in this paper was partially funded by the German Federal Ministry for Economic Affairs and Climate Action under support code 20M1911E. The responsibility for the content of this paper lies with the author.

Supported by:

Federal Ministry for Economic Affairs and Climate Action

on the basis of a decision by the German Bundestag

Thanks are due to the whole VAST development team for the support in the development activities and the ongoing extension of the modeling capabilities of VAST.

7. REFERENCES

[1] N. Roh, D. Park, and S. Oh. Investigation on Loss of Tail-rotor Effectiveness of Helicopter with Ducted Fan Tail Rotor. In *44th European Rotorcraft Forum*, Delft, The Netherlands, September 2018.

[2] N. Roh, S. Oh, and D. Park. Aerodynamic Characteristics of Helicopter with Ducted Fan Tail Rotor in Hover under Low-Speed Crosswind. *International Journal of Aerospace Engineering*, 2020(1), 2020.

[3] T. Zhang. *Numerical investigation of ducted propellers for novel rotorcraft configurations*. Phd thesis, University of Glasgow, 2022.

[4] J. Sun, K. Yonezawa, and H. Liu. Investigation of the Ducted-Propeller Effects on Aeroacoustic Performance using Phase-Locked PIV. In *49th European Rotorcraft Forum*, Bückeburg, Germany, September 2023.

[5] N. Stadlmaier, D. Redmann, F. Hirsch, and V. Zappek. Four-Step Simulation Toolchain to Assess the Effectivity of Noise Reduction Measures for Shrouded Tail Rotors. In *47th European Rotorcraft Forum*, United Kingdom, September 2021.

[6] H. Glauert. A General Theory of the Autogyro. Technical Report ARC R&M 1111, 1926.

[7] F. B. Gustafson and A. Gessow. Effect of Rotor Tip Speed an Helicopter Rotor Performance and Maximum Forward Speed. Technical Report ARR L6A16, NACA, 1946.

[8] J. G. Leishman. *Principles of Helicopter Aerodynamics*. Cambridge University Press, New York, NY, 2nd edition, 2006.

[9] B. G. van der Wall. *Grundlagen der Hubschrauber-Aerodynamik*. Springer-Verlag, Berlin Heidelberg, Germany, 2015.

[10] B. D. Kothmann. *High-frequency directional axis dynamics of helicopters with ducted tail rotors*. PhD thesis, Princeton University, May 2000.

[11] J. L. Pereira. *Hover and Wind-Tunnel Testing of Shrouded Rotors for Improved Micro Air Vehicle Design*. PhD thesis, University of Maryland, College Park, 2008.

[12] C. Stahlhut. Aerodynamic Performance Modeling of Ducted Fans and Shrouded Propellers for Preliminary Design. In *AHS International Forum 70*, Montreal, Canada, May 2014.

[13] P. Krämer. *Hybridmodellierung und Systemidentifizierung der nichtlinearen Hubschrauber-Flugdynamik*. PhD thesis, TU Braunschweig, Braunschweig, Germany, 2006.

[14] S. Bölk, A. Masi, and F. Scorcelletti. AW09 Tail Rotor System Control Authority Assessment. In *49th European Rotorcraft Forum*, Bückeburg, Germany, September 2023.

[15] D. J. Pickles, D. Zagaglia, A. Busse, and R. B. Green. Vortex ring state of a shrouded rotor: an experimental survey. *Experiments in Fluids*, February 2023.

[16] J. Hofmann, M. Kontak, M. Mindt, and F. Weiß. VAST - Versatile Aeromechanics Simulation Platform for Helicopters. In *Deutscher Luft- und Raumfahrtkongress 2020*, Aachen, Germany, September 2020.

[17] M. L. Buhl Jr. New Empirical Relationship between Thrust Coefficient and Induction Factor for the Turbulent Windmill State. August 2005.

[18] B. Michels and P. Seelemeyer. Vast as a generic, modular aeromechanics code for wind turbine simulation. *Journal of Physics: Conference Series*, 2767(5):052023, June 2024.

[19] L. Prandtl and A. Betz. Schraubenpropeller mit geringstem Energieverlust. In *Vier Abhandlungen zur Hydrodynamik und Aerodynamik*, pages 88–92. Göttingen, Germany, 1927.

[20] T. R. Goodman. The Tip Correction for Wind-Tunnel Tests of Propellers. *Journal of the Aeronautical Sciences*, 23(12):1094–1098, 1956.

[21] M. Mindt. Merging an Analytical Aerodynamic Model for Helicopter Applications With a State-Space Formulation for Unsteady Airfoil Behavior. In *67. Deutscher Luft- und Raumfahrtkongress*, Friedrichshafen, Germany, September 2018.

[22] F. A. Weiß, J. Merlis, R. Lojewski, J. Hofmann, and M. Röhrig-Zöllner. Rotor blade modeling in a helicopter multi body simulation based on the floating frame of reference formulation. In *48th European Rotorcraft Forum*, Winterthur, Switzerland, September 2022.

[23] R. M. Grose. Wind Tunnel Tests of Shrouded Propellers at Mach Numbers from 0 to 0.60. Technical Report WADC TR58-604, United Aircraft Corporation, East Hartford, Connecticut, December 1958.

[24] H. Glauert. The Effect of Compressibility on the Lift of an Aerofoil. *Proceedings of the Royal Society*, A118:113–119, 1928.